PCCP

ROYAL SOCIETY OF CHEMISTRY

PAPER

Cite this: *Phys. Chem. Chem. Phys.*, 2023, **25**, 5510

Molecular dynamics study on thermal conductance between a nanotip and a substrate under vertical forces and horizontal sliding

Qiangsheng Sun,[a] Wenxiang Liu,[a] Dezhao Huang,[a] Xiaona Huang,[a] Shen Xu,[b] Jianmei Wang, *[a] Zhijiang Ye,[c] Xiaosun Wang,*[a] Shijing Wu[a] and Yanan Yue *[ac]

The heat transfer between a nanotip and its substrate is extremely complex but is a key factor in determining the measurement accuracy in tip-assisted nanomanufacturing and thermometry. In this work, the heat transfer from the nanotip to the substrate during sliding is investigated using molecular dynamics simulations. Interfacial interaction and bond formation are analyzed during the sliding process. The results show that the increase of vertical force would greatly improve the interface thermal conductance between the nanotip and the substrate. It is found that more bonds are formed and there are larger contact areas at the interface. In addition, we found that the thermal conductivity of the nanotip is another obstacle for heat transfer between the tip and substrate and it is greatly limited by the nanotip diameter near contact which is close to or even smaller than the phonon mean free path. Meanwhile, the dynamic formation and breakage of the covalent bonds during the sliding could gradually smoothen the tip apex and enhance the thermal transport at the interface. This work provides guidance for the thermal design of a nanotip-substrate system for nanoscale thermal transport measurements.

Received 6th October 2022,
Accepted 9th January 2023

DOI: 10.1039/d2cp04655e

rsc.li/pccp

1. Introduction

Tip-assisted nanomanufacturing and thermometry, such as scanning probe lithography,[1] scanning thermal microscopy[2,3] and scanning probe microscopy,[4,5] are effective tools for visualizing and characterizing nanoscale systems due to the high spatial scanning resolution, thermal property detection and local processing.[3,6] However, precise fabrication and quantitative measurements of the thermophysical properties are still challenging, especially when the dimensions approach the nanoscale size.[7–9] There has been extensive research regarding the temperature distribution of a tip-substrate system which is determined by the heat dissipation within the sample and across the interface,[10–12] while the former depends on the intrinsic thermal conductivity of the sample and the latter is influenced by the thermal contact between the tip and the sample surface. In tip-assisted nanomanufacturing, higher tip processing temperature and more heat diffusion to the substrate can be achieved by optimizing the heat transfer within the tip and the contact conditions between it and the substrate to reduce thermal contact resistance. When measuring the temperature at the contact point between the tip and the substrate, accurate thermal contact resistance and the thermal conductivity of the tip are extremely important to derive the contact point temperature by establishing the thermal resistance and heat flow network of the tip-substrate system. The main challenge is the thermal resistance of the tip-substrate interface from the nature of contact,[13–15] which strongly limits the precision of nanoscale manufacturing.

Due to the inherent roughness of the contact surface,[8,16] the thermal contact resistance (TCR) between the nanotip and sample surface arises spontaneously. It is influenced by surface roughness, contact force, intrinsic thermal conductivity, hardness of the sample, *etc.*[9,17] Few methods are available to predict the TCR quantitatively at the nanoscale. In regular tip-assisted nanomanufacturing and thermometry, the TCR estimation is usually based on empirical formulae[18], which is related to the thermal conductivity, microhardness and roughness of the prepared samples. In addition, when the material size is close to or smaller than the phonon mean free path, the size effect becomes a significant factor.[19–21] It can be easily thought that the heat transfer through the nanotip is strongly affected by the boundary scattering of phonons since the nanotip is as small as 10 nm.[4]

[a] *School of Power and Mechanical Engineering, Wuhan University, Wuhan 430072, China. E-mail: jmwang@whu.edu.cn, wxs@whu.edu.cn, yyue@whu.edu.cn*
[b] *School of Mechanical and Automotive Engineering, Shanghai University of Engineering Science, Shanghai 201620, China*
[c] *Department of Mechanical and Manufacturing Engineering, Miami University, Ohio 45056, USA*

Enhancing the heat transport is of great importance for tip-assisted nanomanufacturing and thermometry. Changing contact conditions can effectively reduce thermal resistance and optimize heat transfer in a tip-sample system. Kempf *et al.*[22] increased the contact force in terms of changing the nature of the tip-substrate contact, which reduced the TCR of the probe-sample by 96%, while increasing the measurement sensitivity by more than 2.4 times. Bodzenta *et al.* have conducted quantitative thermal measurements by using a scanning thermal microscope[8,9,23] and pointed out that the thermal resistance between the thermal tip and the sample is the main obstacle to the quantitative calculation of thermophysical properties. Molecular dynamics (MD) simulation is an effective method to explore the effects of nanocontact[2,24,25] on heat transfer in detail,[26–28] because it can present the mechanical and thermal response at the nanoscale in a timely manner and dynamically reveal the evolution of the contacted surface at the atomic level. Many studies have been conducted on friction, wear, adhesion,[2,24,29–33] and conductance across interfaces.[34] However, little works focus on the interface heat transfer, tip size effect and anisotropy of the tip-substrate system.

This work explores the correlation between the interfacial contact mode and the interface thermal conductance (G) of the silicon-based nanotip and silicon substrate system. The contact mode at the interface is studied firstly, including the interface bonding, contact area, and the contact surface phonon behavior. Then, the thermal properties across the interface and inside the nanotip under different contact forces are studied. Our study provides insights into the mechanisms of thermal transport enhancement in the tip-substrate system during sliding and could potentially benefit the nanofabrication and electronic applications.

2. Methodology

2.1 Configuration

The configuration of the whole system is illustrated in Fig. 1, which consists of a diamond silicon substrate and a silicon tip in contact with the (111) surface of the diamond silicon. The contact surface of the substrate is about 12 nm × 12 nm and the thickness is 3 nm. Meanwhile, the profile of the tip is[35] described in cylindrical coordinates as in the following equation:[36]

$$z = \frac{r^N}{NQ} \quad (1)$$

where z is the vertical coordinate indicating the height of the tip, N is the power-law index, and r is the radial coordinate. Q is based on the equation, $S^{N-2}R^{N-1}$, where R and S are both dimensionless parameters to describe the effective tip radius and the steepness of the tip profile, which are independent of N. In this study, the values of N, S and R are chosen as 5, 1 and 2.5, respectively. In terms of the parameter N, the best fit of the power-law curve in the experiment is at either $N = 2$ or $N = 3$. $N = 5$ is employed since the tip used in simulations is smaller than that in experiments,[29] which results in significantly fewer atoms in contact with the substrate in simulations. To better approximate the real situation at contact, a larger N is used to allow more atoms to contact with the substrate. Due to ambient exposure to air, the silicon tip, like typical diamond crystals, is largely passivated by hydrogen, and hydrogen atoms will adhere thinly to the surface of the silicon tip.[2,29,37] In addition, the silicon surface is susceptible to oxidation,[38,39] and a 0.7–0.8 nm thick oxide layer[40] will exist. Other contaminants, especially water and hydrocarbons,[29] may also be present in the experiment, and these can all affect the heat transfer across the interface of the silicon tip. The focus of this study is on the investigation of the effect of sliding on the tip-substrate heat transfer. Therefore, the influence of hydrogen atoms, oxygen atoms and contaminants on heat transfer is neglected in this simulation, and an idealized pure silicon model is developed. It is worth mentioning that, before the simulation, the tip is annealed to facilitate surface reconstruction, especially on the sides of the tip.

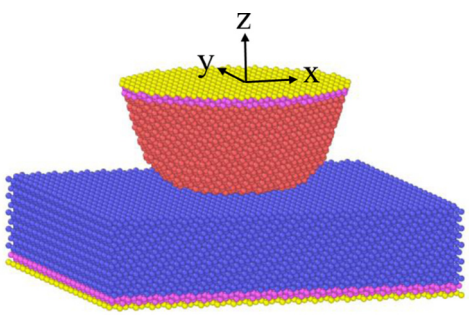

Fig. 1 Atomic configurations of the silicon tip-substrate system. The rigid layers are shown in yellow and the thermostatic regions are shown in purple.

2.2 Simulation of approach and horizontal sliding

All MD simulations in this work are performed using the open-source Large-scale Atomic/Molecular Massively Parallel Simulator (LAMMPS).[41] The reactive force-field potential (ReaxFF) recently updated for the Si/C/H system and optimized for Si surfaces[42,43] is used to describe interatomic forces which is suitable for studying the friction, contact and adhesion processes[44] due to the capability of describing the bond binding and breaking. The cut-formed tip is reconstructed to the most stable configuration through energy minimization based on the conjugate gradient minimization scheme. Then, the approach process of the tip-substrate system is conducted in the following step. The system is first thermalized in the canonical ensemble (NVT) at 300 K for 25 ps so that the temperature distribution of the whole system is uniform and maintained at 300 K. Then the whole system is relaxed in the microcanonical ensemble (NVE) for 30 ps to ensure that the system reaches equilibrium.

Before the approach simulation, the distance between the tip and substrate is 1.0 nm. Then, a constant downward velocity of 0.040 nm ps^{-1} is applied to the rigid layer of the tip (yellow atoms shown in Fig. 1) until a preset target load is achieved. During the simulation, a Langevin thermostat is employed to maintain the temperature at 300 K[45] (purple atoms in Fig. 1). Force–displacement curves during the silicon tip approach are

shown in Fig. 2(a). In the absence of Si–Si bond formation, the force curve is smooth with a single, well-defined minimum, as demonstrated in a previous study.[46] Once a covalent bond exists between the tip and the substrate, the force profile appears with multiple extremes at the beginning of the contact,[2] complicating the force–displacement curve. During this approaching process, the atomic stresses on each atom are calculated and shown in Fig. 2(b–e). It should be noted that the attraction and adhesion between the tip and the substrate result in the occurrence of tensile stresses (as shown in Fig. 2(c)). In Fig. 2(d and e), the compressive forces dominate as the tip approaches the substrate and its distribution is discontinuous at the nanoscale contact.[42,47–49]

To study the effect of sliding and friction loss of the tip on heat transfer, the tip slid for 24.0 nm at a horizontal speed of 0.045 nm ps^{-1} under a constant vertical load of 5.0 nN, which was referenced from studies related to tip friction.[24,50] Applying a horizontal velocity to the tip as shown by the vector $\boldsymbol{v}$ in Fig. 10 causes the tip to move 1 and 2 units in the x and y directions, respectively, at the same time. This allows the tip to slide a longer distance before it encounters the previously probed region, hence, reducing computational costs.

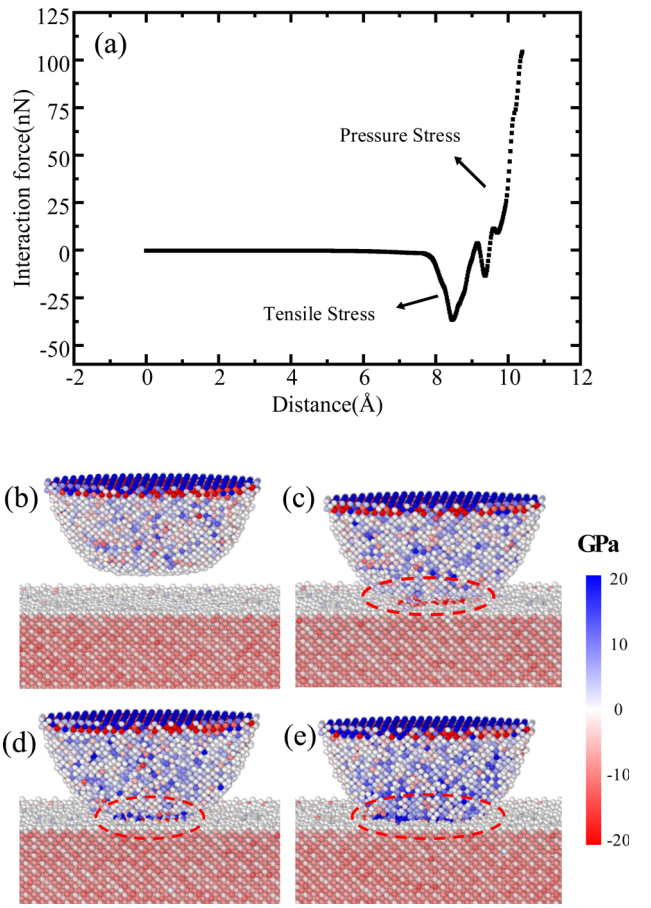

Fig. 2 (a) Force–displacement curves during the silicon tip approach. (b–e) Stress maps of the tip-substrate system at various points during the approach.

2.3 Transient pump–probe method

The transient pump–probe method[51,52] is used to investigate the G between the tip and substrate, due to its advantage of being able to calculate the thermal conductance between irregular interfaces. To begin with, the system is conducted in the NVT ensemble at 300 K for 25 ps to achieve a consistent temperature. Then the whole system is relaxed in NVE for 20 ps to ensure total energy conservation. Once the system reaches thermal equilibrium, a 60 fs ultrafast thermal impulse is applied to the tip. The temperature of the tip increases to 528 K immediately after the aforementioned heat pulse heating, while the temperature of the substrate remains constant. During the subsequent thermal relaxation, heat transfer across the interface is the only way to dissipate the thermal energy of the silicon tip, and the G is then calculated using the following equation:

$$\frac{\mathrm{d}E_{\mathrm{tip}}}{\mathrm{d}t} = G(T - T_{\mathrm{tip}}) \tag{2}$$

where E_{tip}, A, T_{tip} and T_{sub} are the total energy of the tip, the heat transfer area, and the temperatures of the tip and the substrate, respectively. The integral form of eqn (2) is expressed as:

$$E_{\mathrm{t}} = E_0 + G \cdot \int_0^t (T - T_{\mathrm{tip}})\mathrm{d}t \tag{3}$$

where E_{t} denotes the tip's energy that changes with time during the thermal relaxation, and E_0 is the initial value. For example, Fig. 3(a) and (b) show the temperature of the substrate and the tip and their energy as a function of time, respectively. The black and red lines characterize the temperatures of the tip and the substrate, respectively (see Fig. 3(a)). Obviously, the temperature difference decreases with time, implying that the tip and the substrate are continuously exchanging heat, which subsequently converges after 30 ps. Energy relaxation with time is fitted, and the result is shown using the green line in Fig. 3(b). At the beginning portion of the energy curve, there is a small mismatch between the fitting curve and the calculated E_{t} which is because, after 60 fs ultrafast heating, the kinetic and potential energies are in a non-equilibrium state. However, the observed fitting mismatch at the initial portion will not affect the overall fitting result since it lasts only for several picoseconds. The fitting curve in Fig. 3(b) matches perfectly with the energy relaxation curve simulated by MD, which also verifies the reasonableness of this method to calculate G. In addition, the temperature difference $\Delta T = T_{\mathrm{top}} - T_{\mathrm{bot}}$ drives the thermal transport of the tip to the substrate, resulting in energy decay of the tip. The energy change ($\Delta E = E_{\mathrm{t}} - E_0$) of the tip is plotted against $\int (T_{\mathrm{top}} - T_{\mathrm{bot}})\mathrm{d}t$, and it can be found that the energy change is linear with $\int (T_{\mathrm{top}} - T_{\mathrm{bot}})\mathrm{d}t$ (as shown in Fig. 3(c), the slope of the curve characterizes the efficiency of heat transfer across the interface at different temperatures). It can be seen that the heat transfer is very stable, and G can be obtained by fitting the above curve. In addition, the final results are averaged from 5 independent simulations to reduce error.

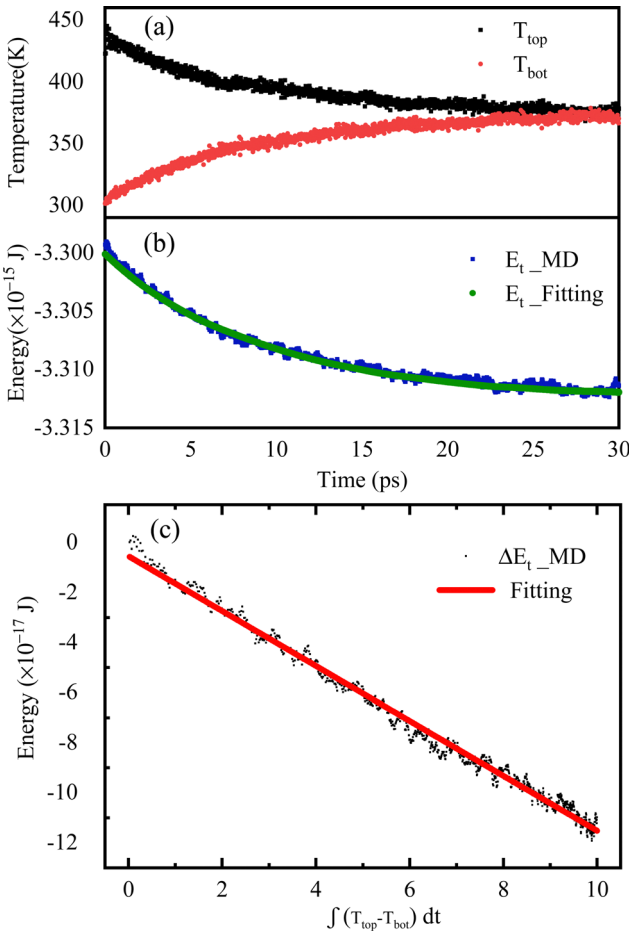

Fig. 3 Schematic diagram of the transient heating method for calculating the interfacial thermal conductance. (a) Temperature profiles of the tip and substrate. (b) Energy relaxation and its fitted curves. (c) Calculation of the interfacial thermal conductance by linear fitting.

2.4 NEMD method to measure thermal conductivity

The purpose of NEMD is to establish the temperature gradient to calculate the thermal conductivity of the nanotip. In this simulation, the system is firstly relaxed in a NVT ensemble and the temperature is maintained at 300 K for 40 ps using a Nose/Hoover temperature thermostat. The NVE ensemble is used for 50 ps to check the system temperature and the energy equilibrium.

Once the equilibration is reached, the Langevin thermostat is applied to the ends of the model, which represents the heat source and heat sink (shown as purple and blue areas in Fig. 4(a)), and the temperatures of those are set at 330 K and 270 K, respectively, as shown in Fig. 4(b). The heat flux is obtained from the energy exchange between the system and the heat sink over time, which is calculated as follows.

$$J = \frac{\mathrm{d}Q}{\mathrm{d}t \cdot A} \tag{4}$$

where $\mathrm{d}Q/\mathrm{d}t$ represents the energy exchange rate of the system with the heat sink and the heat source (the slope of the line shown in Fig. 4(c)) and A is the heat transfer area. Then, the

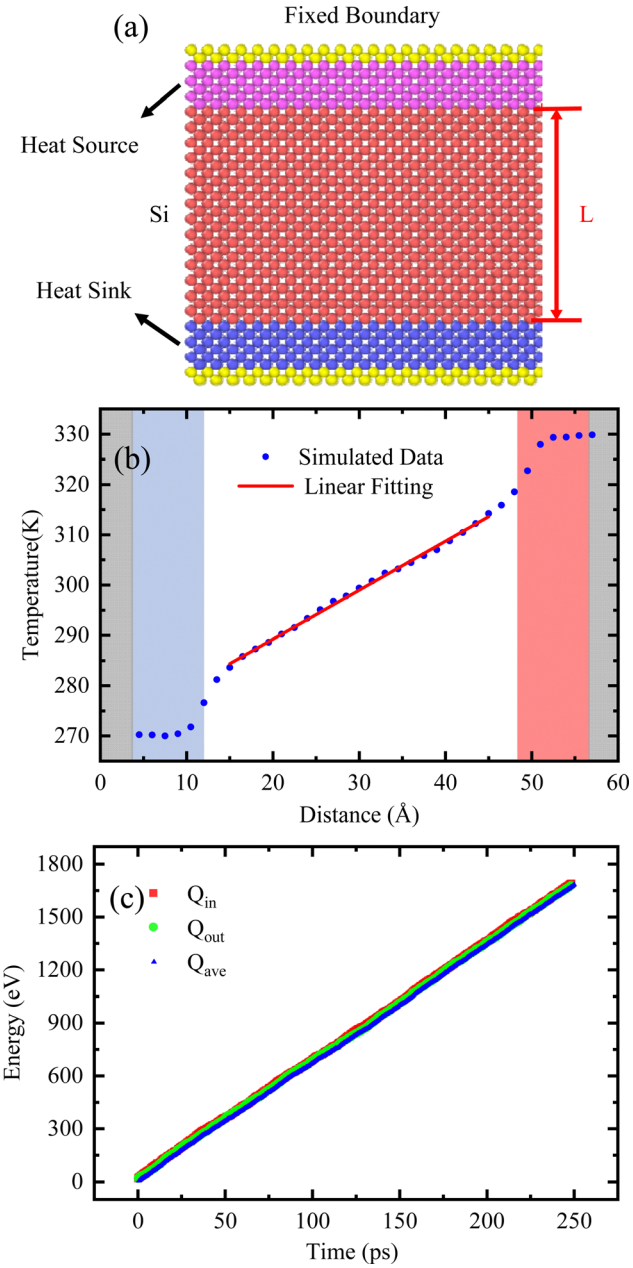

Fig. 4 (a) Structural diagram of the simulated domain including the heat source, the heat sink (8 Å thickness), and the heat transfer region of thickness L between them, and the fixed region (3 Å thickness). (b)Temperature profile along the heat flux direction in thermal equilibrium. Gray, blue and red represent the fixed, heat sink and heat source areas respectively. (c) Energy taken out of or added to the heat sink and heat source regions.

thermal conductivity can be calculated from the following equation:

$$k = \frac{\mathrm{d}Q/(\mathrm{d}t \cdot A)}{\mathrm{d}T/\mathrm{d}x} \tag{5}$$

where $\mathrm{d}T/\mathrm{d}x$ is the rate of temperature change along the heat flux direction (linear fitting of the temperature distribution, shown in Fig. 4(b)).

3. Results and discussion

3.1 Effect of contact force on G

As different contact forces are applied to the interface between the tip and substrate, the contact area and bonding between them will change accordingly. The transient pump–probe method is used to characterize the G of the tip-substrate system, and the results are shown in Fig. 5. In the absence of the load, the tip and substrate are in contact through van der Waals force, and the atoms constantly vibrate to exchange heat. With the increasing contact force, Si–Si bonds are gradually formed, and the contact area also increases. The G increases from 6.64×10^{-9} W K^{-1} at −11 nN to 1.12×10^{-8} W K^{-1} at 104 nN.

This increase can be explained by analyzing the contact area and the bond formation which is affected during the sliding process and strongly related to the interface thermal transport. Here, the bonding or not is characterized based on the distance between two atoms which has a value of 0.2775 nm,[42] which is halfway between the minimum and maximum covalent bonding of Si in the ReaxFF potential and represents a reasonable limit for the range of covalent bonding. Typically, three criteria (*i.e.*, force, potential energy, and distance) are used to determine whether two atoms are in contact. In this study, the atoms forming the Si–Si bond are considered to be in contact. In previous work of Valentini[53] *et al.*, the linear relationship between the square of the contact radius and the contact strain verified that the classical concept of the contact area holds up at the nanoscale. To calculate the contact area, it is common to find a shape that encloses all atoms in contact and define its area as the nanoscale equivalent of the contact area. In this study, the smallest circle[48,54] containing all contact atoms is used to calculate the contact area (the dashed line in Fig. 6(a) shows the equivalent contact area).[34,55,56]

As the contact force between the tip and substrate increases from −11 nN to 104 nN, the number of bonds at the interface and the radius of contact area monotonously creep up from 69.8 to 173.8 and from 1.61 nm to 2.33 nm, respectively (Fig. 6(b)). The higher contact force shortens the distance between tips and substrates, giving rise to an increased opportunity for bonding. As expected, the increased bond number directly leads to an increased G. To further understand the relationship between G and the bond formation, we defined the average thermal conductance per bond ($G_{ave} = G_0/N_{bond}$)

$$G_{ave} = \frac{G_0}{N_{bond}} \tag{6}$$

where G_{ave} denotes the contribution of each bond to the heat

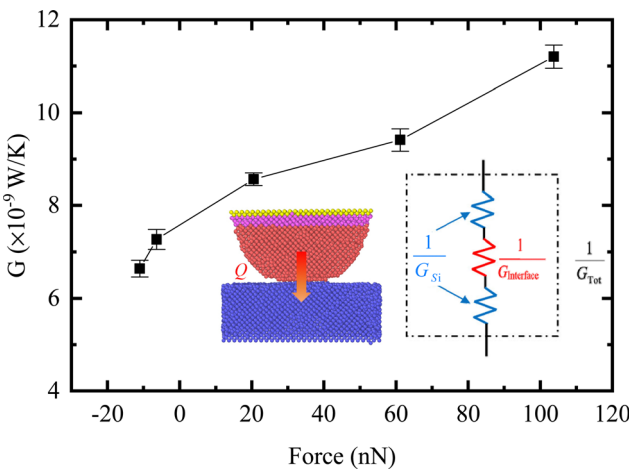

Fig. 5 Interfacial thermal conductance between the tip and substrate as a function of contact force. (The inset shows the schematic of the thermal circuit network for tip-substrate system.)

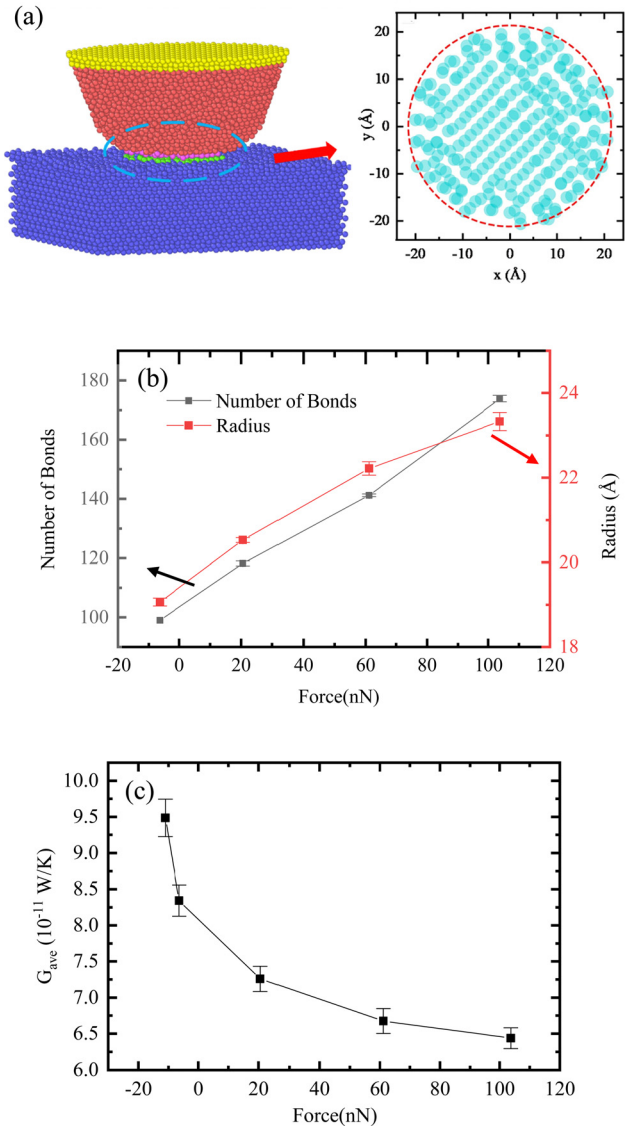

Fig. 6 (a) Diagram of contact simulations. The purple and green atoms represent the bonded atoms between the tip and the sample, which are considered to be in contact. The contact area is calculated using the smallest circle that contains all of the touching atoms (see dotted lines in the figure). (b) The number of interfacial Si–Si bonds and the contact area between the tip and substrate under different contact forces. (c) The average thermal conductance between the tip and substrate as a function of contact force, which represent the contribution of a bond on the contact surface to the heat transfer.

transfer across the interface. Fig. 6(c) shows the results of G_{ave} under different contact forces. As the contact force between the tip and the substrate increases, G_{ave} shows a decreasing trend. That is, when the contact force increases, the overall thermal conductance is enhanced because of the increased bonds and enlarged contact area. However, the thermal conductance per bond decreases. This is because the phonon behaviors of the material are different under different contact forces.

To explain the reason for the reduction in G_{ave} mentioned above, the phonon behavior analysis is given which is important to reveal the mechanism of heat transfer.[57] The phonon density of states (PDOS) can be calculated by performing fast Fourier transform (FFT) on the velocity autocorrelation functions (VACF):

$$F(\omega) = \frac{1}{\sqrt{2\pi}}\int_{-\infty}^{+\infty}\frac{\langle v(0)\cdot v(t)\rangle}{\langle v(0)\cdot v(0)\rangle}e^{i\omega t}\mathrm{d}t \quad (7)$$

The higher the F value of the phonon with frequency ω, the more vibrational states it occupies. In contrast, if the value of F is zero, it means that there are no phonons of frequency ω in the system. The overlap of PDOS is a crucial factor to understand the interfacial thermal transport, and its interrelationship with the contact force needs to be explored. To quantitatively explain the previously discussed results, an overlap factor *(S)* is calculated and expressed as:

$$S = \frac{\int_{-\infty}^{+\infty}F_1(\omega)F_2(\omega)\,\mathrm{d}\omega}{\int_{-\infty}^{+\infty}F_1(\omega)\,\mathrm{d}\omega\int_{-\infty}^{+\infty}F_2(\omega)\,\mathrm{d}\omega} \quad (8)$$

where F_1 and F_2 are the PDOS of the tip and the top region of the substrate. The overlap factor represents the degree of phonon coupling, and a larger value means a stronger phonon coupling between the tip and the substrate, resulting in a higher G.

Fig. 7(a–c) shows the PDOS of the tip and the top region of the substrate under a contact force of 20 nN, 60 nN, and 100 nN. The PDOS of the tip decreases and migrates to the high frequency region (red shift) with contact force, while the PDOS of the substrate is not sensitive to the contact force. The overlap factor decreases monotonically from 0.0696 to 0.0681 with the increase of contact force, indicating the weakened phonon coupling and interfacial thermal transfer leading to a decreased average thermal conductance. In addition, the phonons migrate to the high frequency area, and phonon scattering is enhanced, as illustrated in Fig. 7(d). It weakens the heat transport across the interface and raises the decrease in the average thermal conductance. At the same time, with the increase of contact force, there are a lot of silicon lattice dislocations[58] on the contact surface, and the amorphous phase of silicon appears,[59,60] which will reduce the thermal conductivity and thermal conductance of the contact surface.[61]

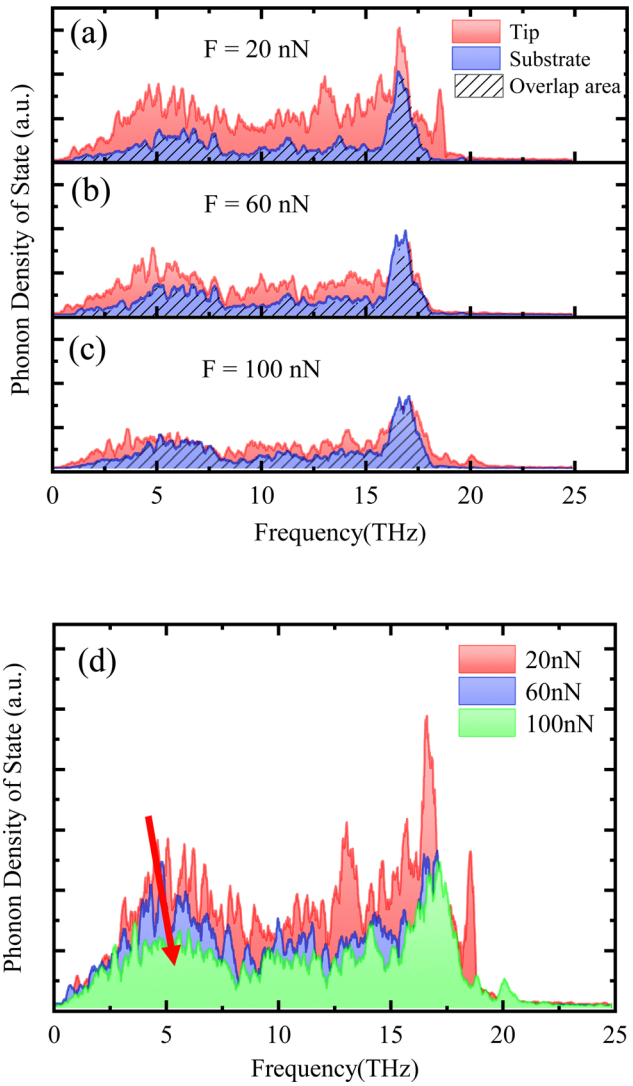

Fig. 7 (a–c) PDOS of the silicon tip and the top region of the substrate at different contact forces. The overlap area decreases monotonically with an increasing contact force, indicating the weakened phonon couplings and decreased the average thermal conductance. (d) PDOS of the silicon tip at different contact forces.

3.2 Heat transfer inside the tip

The nanotip is tapered with a variable cross-section of tens of nanometers, resulting in the size effect and anisotropy, showing different physical properties and special functions from bulk materials. NEMD simulation is performed to study heat transfer inside the tip. A localized Langevin thermostat is used in the upper atom (purple atom) and the lower atom (green atom) to maintain their temperatures at 330 K and 270 K, respectively, with a certain temperature difference between them (the model diagram is inserted in Fig. 8(a)). After equilibration, the tip-substrate temperature distribution is shown in Fig. 8(a).

In Fig. 8(a), there is a huge temperature jump at the two surfaces with contact between the tip and the substrate, indicating that the thermal contact resistance is the largest obstacle in the heat transfer process. In the substrate, the temperature gradient is an inclined straight line with a constant slope. However, the cross section of the tip changes continuously along the direction of heat conduction, resulting in a great change of its temperature gradient. To explore whether the obvious tip temperature change is caused by the change of heat

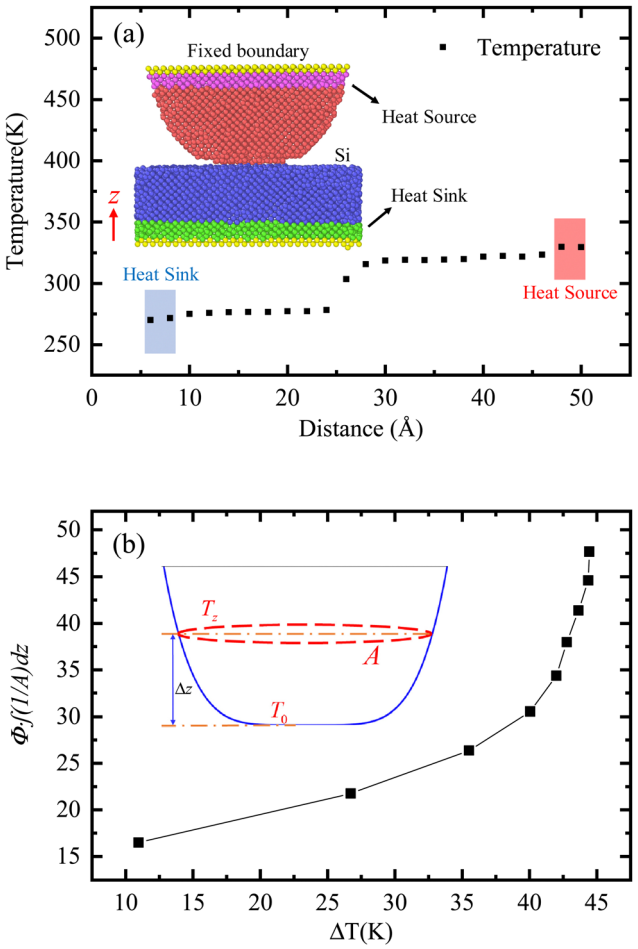

Fig. 8 (a) Temperature profile along the z direction in thermal equilibrium. (The inset shows the model structure of the tip-substrate system. Fixed boundary, heat source and heat sink are shown in yellow, purple and green respectively.) (b) The left side of eqn (9) varies with temperature difference ($T_z - T_0$) in the right, showing that the two are not linear. The slope of the curve increases with the increase of the cross section area, indicating that the thermal conductivity of the tip also increases. (The inset shows the mathematical model of the tip).

transfer area or due to the size effect (physical properties of materials change with the size), the Fourier heat transfer formula is integrated in the Z direction (heat transfer direction) as follows:

$$\phi = -k \cdot A \cdot \frac{\mathrm{d}t}{\mathrm{d}z} \tag{9}$$

$$\phi \cdot \int_0^z \frac{1}{A}\mathrm{d}z = -k(T_z - T_0) \tag{10}$$

where φ, k, and A are the heat flux, thermal conductivity and cross-sectional area, respectively. T_0 and T_z are the temperatures at the tip top and a distance of z away from the top. Assuming that the thermal conductivity k is constant, the left side of eqn (10) should be linear with the temperature difference ($T_z - T_0$) on the right. If not, it means that k changes with the location z. A nonlinear relationship between $\phi \cdot \int_0^z 1/A\,\mathrm{d}z$ and temperature difference is found (see Fig. 8(b)). The slope of the curve means the thermal conductivity at different locations which increases with the cross-sectional area, substantiating the existence of the size effect.

To quantitatively study the effects of the cross-sectional area on the thermal conductivity of the nanotip, a column structure with a cross-section radius ranging from 10–60 Å and a fixed height of 60 Å is established (see Fig. 9(a)). Similarly, NEMD is performed to calculate the thermal conductivity, and the results are shown in Fig. 9(b). When the size of Si is small enough, the boundary scattering becomes the dominant scattering mechanism. The degree of boundary scattering falls with increasing size. The diffusive phonon-boundary scattering process leads to a decrease in the thermal conductivity. Hence, as the cross-sectional radius increases from 10 to 60 Å, the thermal conductivity increases from 0.78 to 2.74 W m^{-1} K^{-1}. It is also proved that the thermal conductivity of the tip is gradually enhanced from the top to the root.

3.3 Effect of tip wear on heat transfer across the contact surface

During the measurement in experiments, the thermal probe contacts the sample surface and captures the temperature feedback to obtain the local thermal characteristics and realize nano-manufacturing.[2,30] As the silicon tip slides across the sample surface, Si–Si bonds are formed across the interface and Si atoms are pulled out of the tip, which then undergoes

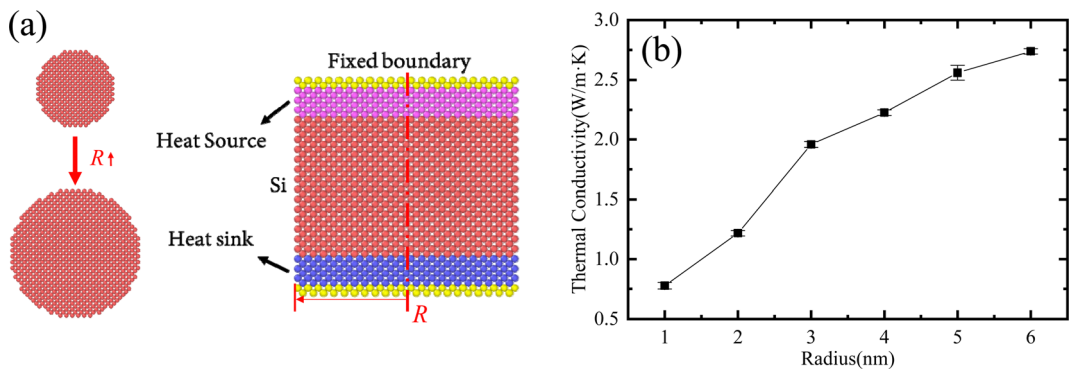

Fig. 9 (a) Simulation model for the column structure. Fixed boundary, heat source and heat sink are shown in yellow, purple and blue respectively. (b) Thermal conductivity as a function of radius of the model.

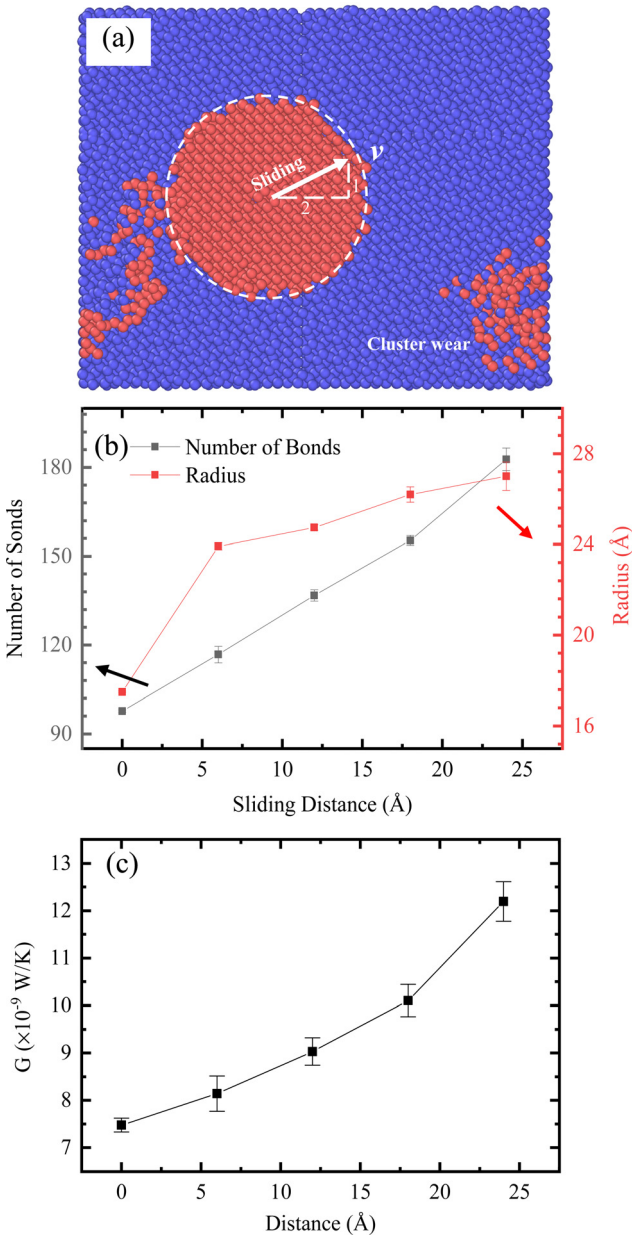

Fig. 10 (a) Top view of the wear simulation after the silicon tip slides 12 nm on the substrate. Illustration of the increased sliding distance without increasing the simulated size by sliding the tip at an angle on the substrate to achieve no coverage of the previously generated wear debris. (b) The number of interfacial Si–Si bonds and the contact area between the tip and substrate after different sliding distances. (c) Interfacial thermal conductance as a function of sliding distance.

atomic-level wear.[50,62] With longer sliding distances, the number of bonds formed increases, along with a larger contact area. Furthermore, the bonds formed at the contact interface are asymmetrically distributed around the silicon tip, which depends mainly on the viscous forces and the direction of sliding.[62] It is worth mentioning that the bonding distribution indicates different tribological behaviors, chip formations and tip's tails displaying the occurrence of abrasive wear and adhesive friction, respectively.

To investigate the possible changes in the tip due to sliding, G, contact area and bonding number were counted after sliding the tip to different distances. Also, given the convenience to discriminate whether the atoms initially belong to the tip or to the substrate, all atoms are assigned to different groups. The tip atom number left on the substrate is counted after sliding. Atoms in red in Fig. 10(a) are tip atoms within 0.5 nm from the substrate surface after 12 nm slide. It can be found that the outermost tip atoms in contact with the substrate have been transferred to the substrate surface, and the number of interfacial bonds always varies as sliding proceeds.

In addition, this simulation also reveals that the formation and breakage of the interfacial bonds during sliding alter the shape of the tip as well as the properties of the tip-substrate contact, which also significantly affects the heat transfer between them. G between the tip and substrate and the corresponding contact conditions (including the bonding and the area of the contact surface) are studied after the tip has been sliding on the substrate for different distances, accompanied by the tip atom separation and tip drop to different degrees. The results are shown in Fig. 10(b and c).

As the tip slides from 0 to 24 nm, the radius of the contact area and the number of Si–Si bonds on the contact surface increase from 1.75 nm to 2.70 nm and from 97.6 to 182.8, respectively. This indicates that the contact between the tip and substrate is more sufficient, reducing G from 7.48×10^{-9} W K^{-1} to 1.22×10^{-8} W K^{-1}. During tip-assisted nanomanufacturing and thermometry, the heat transfer between the tip and the substrate can be further optimized. However, the contact area between the two increases and corresponding spatial resolution is reduced. Therefore, in the process of design and use of the tip, attention should be paid to the comprehensive consideration of heat transfer properties and spatial resolution to balance and achieve the best experimental measurement results.

4. Conclusions

A silicon-based nanotip and silicon substrate system is investigated *via* reactive molecular dynamics to explore the correlation between the interfacial contact mode and thermal properties. The interface thermal resistance is the largest obstacle in the heat transport in the tip-substrate system. By increasing the contact force between the probe and the sample by two orders of magnitude, G is increased by more than 168.7%. With the tip sliding on the substrate, more contacts result in the enhancement of cross-interface heat transfer and the increase of G from 7.48×10^{-9} W K^{-1} to 1.22×10^{-8} W K^{-1}. In addition, since the degree of boundary scattering falls with the increasing size, the thermal conductivity of the tip gradually increases from 0.78 W m^{-1} K^{-1} to 2.74 W m^{-1} K^{-1} from the top to the root. This work demonstrates the importance of the nanoscale interfacial mode in the thermal transport at the tip-substrate interface.

Data availability

The data that support the findings of this study are available from the corresponding author upon reasonable request.

Conflicts of interest

There are no conflicts to declare.

Acknowledgements

The authors acknowledge the financial support from the National Natural Science Foundation of China (No. 52076156), the National Key Research and Development Program of China (No. 2019YFE0119900), the Fundamental Research Funds for the Central Universities (No. 2042022kf1020), and the Natural Science Foundation of Hubei Province (Nos. 2021CFB120 and 2022CFB574). The authors appreciate the support from the Supercomputing Center of Wuhan University.

References

1 R. Garcia, A. W. Knoll and E. Riedo, *Nat. Nanotechnol.*, 2014, **9**, 577–587.
2 Z. B. Milne, J. D. Schall, T. D. B. Jacobs, J. A. Harrison and R. W. Carpick, *ACS Appl. Mater. Interfaces*, 2019, **11**, 40734–40748.
3 N. Gachter, F. Konemann, M. Sistani, M. G. Bartmann, M. Sousa, P. Staudinger, A. Lugstein and B. Gotsmann, *Nanoscale*, 2020, **12**, 20590–20597.
4 S. T. Howell, A. Grushina, F. Holzner and J. Brugger, *Microsyst. Nanoeng.*, 2020, **6**, 21.
5 A. Capaccio, A. Sasso, O. Tarallo and G. Rusciano, *Nanoscale*, 2020, **12**, 24376–24384.
6 S. Huxtable, D. G. Cahill, V. Fauconnier, J. O. White and J. C. Zhao, *Nat. Mater.*, 2004, **3**, 298–301.
7 M. Chirtoc, J. Bodzenta and A. Kaźmierczak-Bałata, *Int. J. Heat Mass Transfer*, 2020, **156**, 119860.
8 B. Gotsmann and M. A. Lantz, *Nat. Mater.*, 2013, **12**, 59–65.
9 K. Kyeongtae, C. Jaehun, H. Gwangseok, K. Ohmyoung and J. S. Lee, *ACS Nano*, 2011, **5**, 8700–8709.
10 K. Kloppstech, N. Konne, S. A. Biehs, A. W. Rodriguez, L. Worbes, D. Hellmann and A. Kittel, *Nat. Commun.*, 2017, **8**, 14475.
11 K. Kim, B. Song, V. Fernandez-Hurtado, W. Lee, W. Jeong, L. Cui, D. Thompson, J. Feist, M. T. Reid, F. J. Garcia-Vidal, J. C. Cuevas, E. Meyhofer and P. Reddy, *Nature*, 2015, **528**, 387–391.
12 S. Lefèvre, S. Volz and P.-O. Chapuis, *Int. J. Heat Mass Transfer*, 2006, **49**, 251–258.
13 N. Mosso, U. Drechsler, F. Menges, P. Nirmalraj, S. Karg, H. Riel and B. Gotsmann, *Nat. Nanotechnol.*, 2017, **12**, 430–433.
14 A. Assy and S. Gomes, *Nanotechnology*, 2015, **26**, 355401.
15 D. Pratap, R. Islam, P. Al-Alam, J. Randrianalisoa and N. Trannoy, *J. Phys. D: Appl. Phys.*, 2018, **51**, 125301.
16 B. N. Persson, *J. Phys.: Condens. Matter*, 2014, **26**, 015009.
17 J.-W. Zhao, R. Zhao, Y.-K. Huo and W.-L. Cheng, *Int. J. Heat Mass Transfer*, 2019, **140**, 705–716.
18 M. Bahrami, J. R. Culham, M. M. Yovanovich and G. E. Schneider, *J. Thermophys. Heat Transfer*, 2004, **18**, 218–227.
19 R. S. Prasher and P. E. Phelan, *J. Heat Transfer*, 1998, **120**, 1078–1081.
20 Y. Yue, J. Zhang, Y. Xie, W. Chen and X. Wang, *Int. J. Heat Mass Transfer*, 2017, **110**, 827–844.
21 A. J. McNamara, B. J. Lee and Z. M. Zhang, *Nanoscale Microscale Thermophys. Eng.*, 2010, **14**, 1–20.
22 N. Kempf and Y. Zhang, *Appl. Phys. Lett.*, 2021, **119**, 113902.
23 J. Bodzenta, A. Kaźmierczak-Bałata and K. Harris, *J. Appl. Phys.*, 2020, **127**, 031103.
24 F. Yang, R. W. Carpick and D. J. Srolovitz, *ACS Nano*, 2017, **11**, 490–500.
25 B. Luan and M. O. Robbins, *Nature*, 2005, **435**, 929–932.
26 M. R. Vazirisereshk, S. A. Sumaiya, A. Martini and M. Z. Baykara, *Appl. Phys. Lett.*, 2019, **115**, 091602.
27 W. Liu, X. Huang and Y. Yue, *Int. J. Heat Mass Transfer*, 2023, **201**, 123673.
28 W. Chen, J. Zhang and Y. Yue, *Int. J. Heat Mass Transfer*, 2016, **103**, 1058–1064.
29 R. A. Bernal, P. Chen, J. D. Schall, J. A. Harrison, Y.-R. Jeng and R. W. Carpick, *Carbon*, 2018, **128**, 267–276.
30 Q. Xu, X. Li, J. Zhang, Y. Hu, H. Wang and T. Ma, *ACS Appl. Mater. Interfaces*, 2017, **9**, 40959–40968.
31 V. Vahdat, K. E. Ryan, P. L. Keating, Y. Jiang, S. P. Adiga, J. D. Schall, K. T. Turner, J. A. Harrison and R. W. Carpick, *ACS Nano*, 2014, **8**, 7027–7040.
32 K. E. Ryan, P. L. Keating, T. D. Jacobs, D. S. Grierson, K. T. Turner, R. W. Carpick and J. A. Harrison, *Langmuir*, 2014, **30**, 2028–2037.
33 Z. Tian, X. Chen and X. Xu, *Int. J. Extreme Manuf.*, 2020, **2**, 045104.
34 X. Hu and A. Martini, *Nanoscale*, 2017, **9**, 16852–16857.
35 D. S. Grierson, J. J. Liu, R. W. Carpick and K. T. Turner, *J. Mech. Phys. Solids*, 2013, **61**, 597–610.
36 T. D. B. Jacobs, K. E. Ryan, P. L. Keating, D. S. Grierson, J. A. Lefever, K. T. Turner, J. A. Harrison and R. W. Carpick, *Tribol. Lett.*, 2013, **50**, 81–93.
37 M. Suri and T. Dumitrică, *Phys. Rev. B: Condens. Matter Mater. Phys.*, 2008, **78**, 081405.
38 J. D. Evans, M. Vynnycky and S. P. Ferro, *J. Eng. Math.*, 2000, **38**, 191–218.
39 M. Suezawa, Y. Yamamoto, M. Suemitsu and I. Yonenaga, *Phys. Rev. B: Condens. Matter Mater. Phys.*, 2009, **404**, 5156–5158.
40 A. G. Silva, K. Pedersen, Z. S. Li and P. Morgen, *Thin Solid Films*, 2011, **520**, 697–699.
41 S. Plimpton, *J. Comput. Phys.*, 1995, **117**, 1–19.
42 J. D. Schall and J. A. Harrison, *J. Phys. Chem. C*, 2013, **117**, 1323–1334.
43 J. D. Schall, G. Gao and J. A. Harrison, *Phys. Rev. B: Condens. Matter Mater. Phys.*, 2008, **77**, 115209.
44 L. Pastewka, P. Pou, R. Pérez, P. Gumbsch and M. Moseler, *Phys. Rev. B: Condens. Matter Mater. Phys.*, 2008, **78**, 161402.

45 H. J. C. Berendsen, J. P. M. Postma, W. F. Vangunsteren, A. Dinola and J. R. Haak, *J. Chem. Phys.*, 1984, **81**, 3684–3690.
46 K. E. Ryan, P. L. Keating, T. D. B. Jacobs, D. S. Grierson, K. T. Turner, R. W. Carpick and J. A. Harrison, *Langmuir*, 2014, **30**, 2028–2037.
47 B. Luan and M. Robbins, *Nature*, 2005, **435**, 929–932.
48 Y. Mo, K. T. Turner and I. Szlufarska, *Nature*, 2009, **457**, 1116–1119.
49 Z. Ye, H. Moon, M. H. Lee and A. Martini, *Tribol. Int.*, 2014, **71**, 109–113.
50 L. Bai, N. Srikanth, E. A. Korznikova, J. A. Baimova, S. V. Dmitriev and K. Zhou, *Wear*, 2017, **372–373**, 12–20.
51 W. Liu, Y. Wu, Y. Hong, B. Hou, J. Zhang and Y. Yue, *Phys. Chem. Chem. Phys.*, 2021, **23**, 19166–19172.
52 J. Zhang, Y. Hong, Z. Tong, Z. Xiao, H. Bao and Y. Yue, *Phys. Chem. Chem. Phys.*, 2015, **17**, 23704–23710.
53 P. Valentini, W. W. Gerberich and T. Dumitrica, *Phys. Rev. Lett.*, 2007, **99**, 175701.
54 S. Cheng, B. Luan and M. O. Robbins, *Phys. Rev. E: Stat., Nonlinear, Soft Matter Phys.*, 2010, **81**, 016102.
55 M. Chandross, C. D. Lorenz, M. J. Stevens and G. S. Grest, *Langmuir*, 2008, **24**, 1240–1246.
56 T. D. B. Jacobs and A. Martini, *Appl. Mech. Rev.*, 2017, **69**, 060802.
57 Y. Zhang, J. X. Cao, Y. Xiao and X. H. Yan, *J. Appl. Phys.*, 2007, **102**, 208.
58 H. Babaei, R. Guo, A. Hashemi and S. Lee, *Phys. Rev. Mater.*, 2019, **3**, 074603.
59 R. Li, E. Lee and T. Luo, *Mater. Today Phys.*, 2020, **12**, 100181.
60 X. Qian, S. Peng, X. Li, Y. Wei and R. Yang, *Mater. Today Phys.*, 2019, **10**, 100140.
61 M. Li and Y. Yue, *RSC Adv.*, 2014, **4**, 23010–23016.
62 T. Ishida, T. Sato, T. Ishikawa, M. Oguma, N. Itamura, K. Goda, N. Sasaki and H. Fujita, *Nano Lett.*, 2015, **15**, 1476–1480.